

Denoising of gravitational wave signals via dictionary learning algorithms

Alejandro Torres-Forné,¹ Antonio Marquina,² José A. Font,^{1,3} and José M. Ibáñez^{1,3}

¹*Departamento de Astronomía y Astrofísica, Universitat de València, Dr. Moliner 50, 46100, Burjassot (València), Spain*

²*Departamento de Matemáticas, Universitat de València, Dr. Moliner 50, 46100, Burjassot (València), Spain*

³*Observatori Astronòmic, Universitat de València, C/ Catedrático José Beltrán 2, 46980, Paterna (València), Spain*

Gravitational wave astronomy has become a reality after the historical detections accomplished during the first observing run of the two advanced LIGO detectors. In the following years, the number of detections is expected to increase significantly with the full commissioning of the advanced LIGO, advanced Virgo and KAGRA detectors. The development of sophisticated data analysis techniques to improve the opportunities of detection for low signal-to-noise-ratio events is hence a most crucial effort. We present in this paper one such technique, dictionary-learning algorithms, which have been extensively developed in the last few years and successfully applied mostly in the context of image processing. However, to the best of our knowledge, such algorithms have not yet been employed to denoise gravitational wave signals. By building dictionaries from numerical relativity templates of both, binary black holes mergers and bursts of rotational core collapse, we show how machine-learning algorithms based on dictionaries can be also successfully applied for gravitational wave denoising. We use a subset of signals from both catalogs, embedded in non-white Gaussian noise, to assess our techniques with a large sample of tests and to find the best model parameters. The application of our method to the actual signal GW150914 shows promising results. Dictionary-learning algorithms could be a complementary addition to the gravitational wave data analysis toolkit. They may be used to extract signals from noise and to infer physical parameters if the data are in good enough agreement with the morphology of the dictionary atoms.

PACS numbers: 04.30.Tv, 04.80.Nn, 05.45.Tp, 07.05.Kf,

I. INTRODUCTION

The epoch-making detections of the transient gravitational-wave (GW) signals GW150914 and GW151226 during the first observing run of the two Advanced LIGO interferometers [1, 2] has marked the start of GW astronomy. GW150914, detected with unexpectedly high signal-to-noise (SNR) ratio (SNR \sim 24) and with a statistical significance greater than 5.1σ , is in excellent agreement with numerical relativity waveforms [3–5] for the final few cycles (chirp), merger (burst) and subsequent ringdown of the coalescence of two stellar-origin black holes (BHs) in a binary system. GW151226, also the result of a binary BH merger, was recovered with similar statistical significance but with a SNR \sim 13. Its initial BH masses, $14.2M_{\odot}$ and $7.5M_{\odot}$, are lower than in the case of GW150914, $35M_{\odot}$ and $30M_{\odot}$. As a result, GW151226 spent almost 1 s in the LIGO frequency band, increasing in frequency and amplitude from 35 to 450 Hz over about 55 cycles. Contrary to GW150914, matched filtering with waveform templates from general relativity was essential to detect GW151226 due to the smaller strain amplitude and the longer time interval [2].

At present, the two Advanced LIGO interferometers are being upgraded. The second observing run (O2) is expected to start in late 2016 with a significant strain improvement. At the same time, the commissioning of the European detector Advanced Virgo [6] is well underway, aiming at start observing in the second half of this year, while the Japanese detector KAGRA [7] is still under construction. Simultaneous observational campaigns of these four detectors, five with the later addition of the recently approved LIGO India, will increase considerably the rate of detections along with their statistical significance and the accuracy of the sky location of each

event [8].

Despite the recent discoveries, noise removal remains one of the most challenging problems in GW data analysis. There exist a number of noise sources that limit the possibilities of detection [9]. The most limiting source of noise for frequencies below a few tens of Hz is gravity gradient noise. Thermal noise due to Brownian motion is dominant at intermediate frequencies, while shot noise, produced by quantum fluctuations of the laser, becomes prominent at frequencies above ~ 150 Hz, difficulting detection above 2 kHz. Nevertheless, searches for gravitational wave bursts up to frequencies of 5 kHz have been performed [10]. These sources of noise are not stationary and the sensitivity of the detectors changes with time. To add more complexity, transient spurious noise signals (glitches) due to instrumental or environmental sources, may potentially disturb astrophysical signals. Glitches might mimic GW signals increasing the false alarm rate and producing a decrease in the detectors' duty cycles. A huge effort in commissioning and detector characterization [11] has been done to reduce the effect of glitches. Improving glitch identification and classification [12, 13] would improve detection efficiency but there will always be a chance for false positives in the detectors.

GW detectors are designed to be sensitive to waveforms produced by different astrophysical mechanisms. Sources can be separated in groups depending on how well-known and modeled their waveforms are. Specific data analysis techniques have been developed for each type of signal (for a review see [14] and references therein). Transient GW signals from compact binary coalescence (CBC), either from binary neutron stars (BNS) or binary black holes (BBH), are well studied and the corresponding waveforms can be calculated with high accuracy. These systems are typically modeled us-

ing the effective-one-body formalism (EOB) [15] which combines post-Newtonian methods [16, 17] with numerical relativity and perturbation theory [18]. This technique allows to generate template banks efficiently. This is the main reason matched-filtering is the most common method for CBC detection [19–21] in which filters correlate signals with templates. A trigger associated with a specific template is generated when the filter output excess a certain threshold. In addition to EOB waveforms, other waveform families are needed to cover as much parameter space as possible (see [22] and references therein).

Matched-filtering becomes however unpractical for well-modeled but continuous sources, like spinning neutron stars, due to the large computational resources it would require. Nevertheless, as such signals are very stable and have long duration, a coherent integration can be performed. In addition, the data from all detectors can be compared, which increases the SNR of this type of events. Roughly speaking there are two main methods to fulfill this comparison, cross-correlation methods and coherent methods [23, 24]. The former directly compare the data streams from a pair of detectors to search for a common signal within uncorrelated noise while the latter generalize the concepts of excess power and cross-correlation to take full advantage of having three or more data streams. The duration and the sky coverage (all-sky or targeted) [25] can vary depending of the type of source which is sought for.

In contrast with the last type of sources, the non-spherical gravitational collapse of massive stars produces a short (\sim ms) duration (prompt) signal (but see [26] for the case of collapsars where the duration of the signal is dominated by the accretion timescale, considerably longer) with a significant power in the kHz frequency band. In addition to core-collapse supernova, other astrophysical sources as cosmic string cusps [27] and BBH mergers, can also produce GW transients or “bursts”. Such signals, in particular core-collapse bursts, can only be modeled imperfectly, and the computational requirements for obtaining the corresponding waveforms from numerical relativity simulations are much larger than in the case of CBC. Therefore, a bank of templates cannot be built with sufficient accuracy to meet the requirements of matched-filtering. For burst signals, the time-frequency analysis of the signal in all the detectors, related to each other with cross-correlation and coherent methods, is the best option. With initial detectors, a complete all-sky, all-time burst search was performed [10] and has also been carried out during Advanced LIGO’s first observing run (O1) [28]. These techniques, used in tandem with electromagnetic observations, can increase the possibilities of identifying a GW burst [29].

The detection confidence of unmodeled astrophysical sources has significantly improved in recent years. In particular, coherent approaches over a network of GW detectors have proven to be very effective [30, 31], increasing the detection confidence of long-duration (above several seconds) burst signals which are insensitive to the presence of most noise transients. In contrast, short-duration bursts are more affected by detector glitches and specific pipelines based on Bayesian inference have been developed to differentiate between signals

and noise transients, namely `coherentWaveBurst` [32], `BayesWave` [33], and `oLIB` [34]. Other approaches, like those of [35, 36], have proven to be effective for estimating physical parameters and for the reconstruction of burst signal waveforms from (Gaussian) noisy environments.

Apart from the standard techniques mentioned in the previous paragraphs, GW data analysis can benefit from the incorporation of new approaches from other fields. Recently, we presented in [37] new methods for denoising GW signals based on L^1 -norm minimization, modeling the denoising problem as a variational problem. These methods have been originally developed and fully tested in the context of image processing where they have been shown to be the best approach to solve the so-called Rudin-Osher-Fatemi denoising model [38].

In this paper we continue the work initiated in [37]. We assume the linear degradation model to solve the denoising problem as the estimation of the recovered signal \mathbf{u} from the relation $\mathbf{f} = \mathbf{u} + \mathbf{n}$ where the measured signal is \mathbf{f} and \mathbf{n} is white Gaussian noise of zero mean. Our approach in [37] consisted in obtaining \mathbf{u} as the unique minimizer of the total variation norm of the signal subject to a fidelity term expressed in terms of the L^2 -norm of the residual, i.e., $\|\mathbf{f} - \mathbf{u}\|_{L^2}^2$. Here, we propose an alternative approach based on the sparse reconstruction of the signal \mathbf{u} over learned dictionaries, built from existing waveform catalogs. The development of models and algorithms for sparse reconstruction of signals over a dictionary has been a subject of great interest in recent years [39–41]. It appears as an alternative to the traditional signal representation based on Fourier decomposition or more modern representations based on wavelets, chirplets, warplets, etc.

Following the terminology introduced by Mallat and Zhang [42] a *dictionary* is a collection of signals (in our case waveforms) of length n called *atoms*,

$$\mathbf{u} = \mathbf{D}\boldsymbol{\alpha}, \quad (1.1)$$

where \mathbf{u} is the signal to be recovered, $\mathbf{D} = [\mathbf{d}_1, \dots, \mathbf{d}_p]$ is the dictionary, which is composed of p atoms of length n , and $\boldsymbol{\alpha} \in \mathbb{R}^p$ is a vector which contains the coefficients of the representation. The atoms are not set to be orthogonal unlike in other decompositions like those based in Principal Component Analysis (PCA), allowing more flexibility in the representation. A dictionary can be complete, if it contains exactly $p = n$ atoms, or overcomplete if $p > n$ atoms. In the latter case the solution vector $\boldsymbol{\alpha}$ is not unique and cannot be obtained by applying simple linear methods. In our work, we use the *basis pursuit decomposition* proposed in [39]. An interesting review of other approaches to solve problem (1.1) can also be found in Ref. [39].

The prototype signals of a dictionary can be chosen as a predefined set of functions, like a Fourier basis (frequency dictionaries), several types of wavelet functions (wavelet dictionaries) or Gabor wavelet decomposition to produce time-frequency dictionaries. However, the idea of using a dictionary learned from data has improved the denoising results considerably [40]. Nowadays, state-of-the-art algorithms for reconstruction and denoising are being developed along this direction [41], and very efficient methods have been devised to

solve the challenging optimization problem inherent to learning dictionaries.

The sparse reconstructions of signals over trained dictionaries we propose in this work are obtained for the same kind of GW trained signals that we did in [37], namely burst signals from a catalog of rotational stellar core collapse [43] and chirp-burst-ringdown signals from a catalog of BBH mergers [5]. Once the dictionaries are set, we demonstrate their utility for the denoising of GW signals embedded in Gaussian noise.

This paper is organized as follows: Section II describes the basic mathematical details of our method, namely the sparse representation and the dictionary learning problems together with the specific formulation we use to solve them. Section III deals with the GW waveform catalogs we employ to assess our method. In Section IV we adapt the general problem to the specific case of GW signals and we obtain the optimal set of model parameters to perform the denoising of given signals. In Sections V and VI we illustrate our technique with a significant sample of test cases. Section VII discusses the performance of our method when applied to the actual signal GW150914. Finally, the conclusions of our work and possible future extensions are presented in Section VIII. Appendix A contains a table with the correspondence between the naming of the GW signals employed in this study and that of the original GW catalogs.

II. MATHEMATICAL FRAMEWORK

A. Sparse Reconstruction over a fixed dictionary

We start from the linear degradation model

$$\mathbf{f} = \mathbf{u} + \mathbf{n}, \quad (2.1)$$

where \mathbf{f} is the measured signal, \mathbf{u} is the GW signal to be recovered and \mathbf{n} is random Gaussian noise. If signal \mathbf{u} is a vector $\mathbf{u} \in \mathbb{R}^n$ one can say that it admits a sparse approximation over an overcomplete dictionary $\mathbf{D} \in \mathbb{R}^{n \times p}$, where each column contains one of the p atoms of length n and $p > n$, when one can find a linear combination of a few atoms from \mathbf{D} that is close to \mathbf{u} . The classical dictionary learning techniques [44, 45] try to solve the variational problem associated with Eq. (1.1) given by,

$$\alpha = \underset{\alpha}{\operatorname{argmin}} \|\alpha\|_0 \text{ subject to } \mathbf{D}\alpha \sim \mathbf{u}, \quad (2.2)$$

where $\|\cdot\|_0$ is the L^0 -norm to assure that we have the solution with the fewest number of nonzero coefficients. The L^0 -norm is just the number of nonzero components of the vector. This constrained variational problem can be formulated as an unconstrained variational problem adding the L^0 -norm term as a penalty term weighted by a Lagrangian multiplier λ ,

$$\alpha = \underset{\alpha}{\operatorname{argmin}} \|\mathbf{D}\alpha - \mathbf{f}\|_2^2 + \lambda \|\alpha\|_0. \quad (2.3)$$

This problem is not convex and is NP-hard (i.e. non-deterministic polynomial-time hard) so, in practice, it cannot be solved in linear time [46]. A problem is in the NP

class if it can be solved in non-deterministic polynomial-time. Algorithms that produce and approximate solutions to this problem have been proposed in the past. The simplest ones are matching pursuit (MP) and orthogonal matching pursuit (OMP) (see [39] and references therein for details).

The variational problem defined by Eq. (2.3) can be reformulated into a convex variational formulation by substituting the L^0 -norm by the nondifferentiable convex L^1 -norm in the total energy. The regularization in the L^1 -norm promotes zeros in the components of the vector coefficient α . This problem can be solved in linear time and the solution found is the sparsest one in most cases. The variational problem thus stands as,

$$\alpha = \underset{\alpha}{\operatorname{argmin}} \|\mathbf{D}\alpha - \mathbf{f}\|_2^2 + \lambda \|\alpha\|_1, \quad (2.4)$$

which is known as *basis pursuit* [39] or *LASSO* [47]. An alternative formulation known as *elastic-net* [48],

$$\alpha = \underset{\alpha}{\operatorname{argmin}} \|\mathbf{D}\alpha - \mathbf{f}\|_2^2 + \lambda_1 \|\alpha\|_1 + \frac{\lambda_2}{2} \|\alpha\|_2^2, \quad (2.5)$$

adds a L^2 -norm penalty for stability reasons, i.e., the calculated approximate representation depends on the data as a Lipschitz function.

To solve the LASSO problem (2.4) we propose a decomposition based on the Split-Bregman (SB) algorithm [49]. The SB algorithm solves very efficiently L^1 -norm minimization problems, like the Rudin-Osher-Fatemi variational model [38], decoupling the L^1 -norm and L^2 -norm terms and solving them alternatively until convergence is reached. In order to achieve this goal we introduce a new independent unknown vector \mathbf{d} to split the minimization with respect to the L^1 -norm. Applying this splitting the problem reads as follows

$$(\alpha, \mathbf{d}) = \underset{\alpha, \mathbf{d}}{\operatorname{argmin}} \|\mathbf{D}\alpha - \mathbf{f}\|_2^2 + \lambda \|\mathbf{d}\|_1 + \mu \|\alpha - \mathbf{d}\|_2^2. \quad (2.6)$$

By iteratively minimizing with respect to α and \mathbf{d} separately, the SB iterative procedure reads as follows

$$\alpha^{k+1} = \underset{\alpha}{\operatorname{argmin}} \frac{\lambda}{2} \|\mathbf{f} - \mathbf{D}\alpha\|_2^2 + \frac{\mu}{2} \|\mathbf{b}^k + \alpha - \mathbf{d}^k\|_2^2, \quad (2.7)$$

$$\mathbf{d}^{k+1} = \underset{\mathbf{d}}{\operatorname{argmin}} \|\mathbf{d}\|_1 + \frac{\mu}{2} \|\mathbf{b}^k + \alpha^{k+1} - \mathbf{d}\|_2^2, \quad (2.8)$$

$$\mathbf{b}^{k+1} = \mathbf{b}^k + \alpha^{k+1} - \mathbf{d}^{k+1}, \quad (2.9)$$

starting with $\mathbf{b}^0 = 0$. The role of the auxiliary vector \mathbf{b} is to enforce the unknowns \mathbf{d} and α be equal when convergence is reached. The iteration process uses a small positive fixed value of μ and it runs over a scale-space that reconstructs the signal as a linear combination of few elements of the dictionary. Since the two parts are decoupled, they can be solved independently. The energy of the first step is smooth (i.e. differentiable) and it can be solved using common techniques as the Gauss-Seidel method. On the other hand, \mathbf{d} can be explicitly computed to optimal values by using the shrinkage operator,

$$\mathbf{d}^{k+1} = \operatorname{shrink}(\mathbf{b}^k + \alpha^{k+1}, 1/\mu), \quad (2.10)$$

$$\text{shrink}(x, \gamma) = \frac{x}{|x|} \max(|x| - \gamma, 0). \quad (2.11)$$

In practice we only use one iteration for the splitting steps and the final algorithm only consists of just one loop (see [49] for a detailed discussion).

B. Dictionary Learning Problem

Up to this point we have considered that the dictionary \mathbf{D} is fixed and we only have to solve the problem of representation. As we want to design the dictionary to fit a given set of GW signals, we start by considering a finite number of training signals, which can be split in m patches of length n , i.e. $\mathbf{U} = [\mathbf{u}_1, \dots, \mathbf{u}_m]$ in $\mathbb{R}^{n \times m}$. In most common problems, the number of training patches m is large compared with the length of each patch, $n \ll m$. In general, the number of atoms in the dictionary is lower than the number of patches, $p \ll m$, because each signal only uses a few elements in \mathbf{D} for the representation.

To obtain the trained dictionary, we need to add the dictionary matrix \mathbf{D} as a variable in the minimization problem

$$\alpha = \underset{\alpha, \mathbf{D}}{\text{argmin}} \frac{1}{n} \sum_{i=1}^m \|\mathbf{D}\alpha_i - \mathbf{u}_i\|_2^2 + \lambda \|\alpha_i\|_1, \quad (2.12)$$

where the summation index i indicates the i -th row of $\alpha \in \mathbb{R}^{p \times n}$ (now a matrix), which contains the coefficients of the sparse representation of each atom in the dictionary. The constraint in \mathbf{D} reads

$$\mathbf{D} \in \mathbb{R}^{n \times p} \text{ subject to } (\mathbf{d}_i^T \mathbf{d}_i) \leq 1 \quad \forall i = 1, \dots, p. \quad (2.13)$$

The whole problem (2.12) is not jointly convex, but convex with respect to either of the two variables, α, \mathbf{D} , keeping the other one fixed. To perform the dictionary update we follow the algorithm proposed by Mairal et al in [51] to which the reader is addressed for details. These authors use a block-coordinate descent method [50] for solving for \mathbf{D} and α_i iteratively,

$$\alpha^{k+1} = \underset{\alpha}{\text{argmin}} \frac{1}{n} \sum_{i=1}^m \|\mathbf{D}^k \alpha_i - \mathbf{u}_i\|_2^2 + \lambda \|\alpha_i\|_1 \quad (2.14)$$

$$\mathbf{D}^{k+1} = \underset{\mathbf{D}}{\text{argmin}} \frac{1}{n} \sum_{i=1}^m \|\mathbf{D} \alpha_i^{k+1} - \mathbf{u}_i\|_2^2 + \lambda \|\alpha_i\|_1 \quad (2.15)$$

The main advantage of this implementation is that it is parameter-free and does not require any learning rate.

III. GRAVITATIONAL WAVE CATALOGS

In the present work we employ the same two catalogs of GW signals used in [37] to assess our method, namely a catalog of signals from relativistic rotational core collapse simulations [43] and a catalog from BBH simulations [5]. In addition, we also consider two extra signals, one from a core

collapse catalog developed by Abdikamalov et al. [52] and a BBH signal from [53]. These last two signals allow us to investigate the ability of our approach to extract independent waveforms using dictionaries built from atoms that do not contain explicit information on the signals to be denoised.

In the core collapse scenario the bulk of gravitational radiation is emitted during bounce, when the quadrupole moment changes rapidly, which produces a burst of GWs with a duration of about 10 ms and a maximum dimensionless amplitude of about 10^{-21} at a distance of 10 kpc. Broadly speaking, GW signals from core collapse exhibit a distinctive morphology characterized by a steep rise in amplitude to positive values before bounce followed by a negative peak at bounce and a series of damped oscillations associated with the oscillations of the newly formed proto-neutron star around its equilibrium solution. We employ the catalog developed by Dimmellemeier et al. [43], who obtained 128 waveforms from general relativistic simulations of rotating stellar core collapse to a neutron star using the `CoCoNuT` code. The core collapse template bank computed by [52] has also been built through axisymmetric simulations with the `CoCoNuT` code. The progenitors investigated have different initial angular momentum distributions in the core and the simulations include a microphysical finite-temperature equation of state, an approximate electron capture treatment during collapse, and a neutrino leakage scheme for the postbounce evolution.

Regarding BBH signals we consider the BBH waveform catalog of Mroué et al [5] which includes the late inspiral, merger, and quasi-normal mode ringdown signals for 174 different models. Those waveforms have been computed using the Spectral Einstein Code (`SpEC`) [54]. In addition we employ the ‘R1’ BBH waveform computed by the GSF group [53] and available at [55]. This waveform includes the late inspiral and merger phases of an irrotational BBH simulation performed with a grid-based numerical code, conformally flat initial data and the BSSN system of equations. The numerical code and techniques are hence different to those used by [5].

IV. DICTIONARY GENERATION AND PARAMETER EVALUATION

A. Dictionary generation

We now turn to describe the process to generate a learned dictionary from the waveforms of both catalogs. The goal is to find the best set of dictionary parameters that produce the best denoising results. As in [37] we find that the results depend critically on the value of the regularization parameter λ selected. The way we build the dictionaries for the burst and BBH catalogs is similar. We divide randomly in three groups both the 128 burst waveform signals of [43] and the first 100 BBH waveforms of [5]. Since the BBH signals of [5] are quite large, we do not use the entire BBH catalog in order to save computational resources. Specifically, the BBH catalog covers binaries with total mass $20M_{\odot}$ and mass ratios up to 1:8,

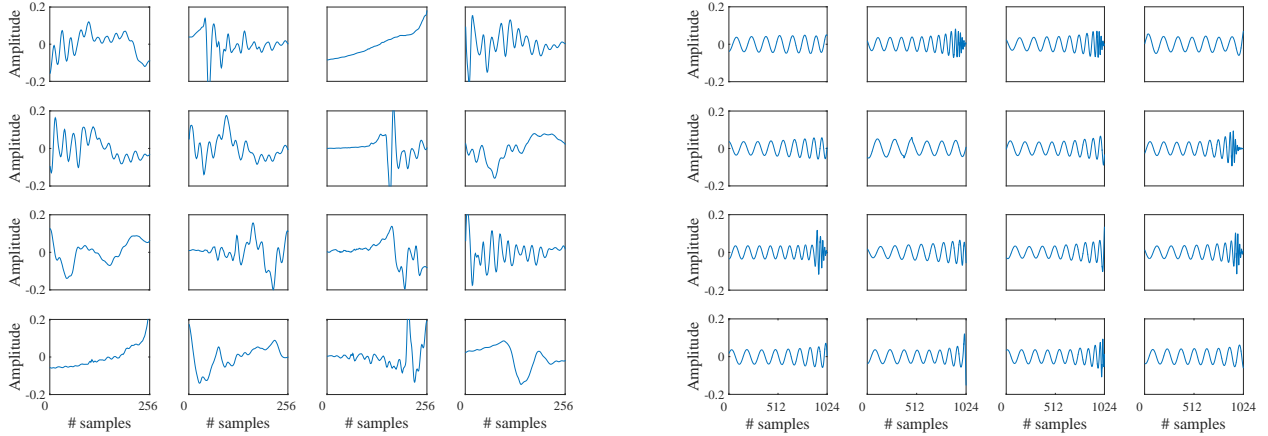


FIG. 1: Random examples of the atoms of both dictionaries, for burst waveforms (left panel) and for BBH signals (right panel). The number of samples is shown in the horizontal axis while the normalized amplitude is shown in the vertical axis.

and so does our dictionary. We then use in either case 80% of the waveforms for training the dictionary, 15% for validation of the method, i.e. to search the best set of parameters, and the remaining 5% to test the algorithm in different situations.

The numerically generated signals are embedded in non-white, Gaussian noise corresponding to Advanced LIGO proposed broadband configuration, provided by the LSC Algorithm Library Suite (LAL) [56]. The frequency ranges from 10 Hz to 8192 Hz (one-sided spectrum). First of all, we resample the waveforms of both catalogs to the Advanced LIGO/Virgo sampling rate of 16384 Hz, zero padded to have the same length. The corresponding signals are also shifted to be aligned with either the minimum peak in the case of bursts or with the maximum peak in the merger part for BBH signals. We select 2048 samples around the corresponding alignment points to train the dictionary. With this length, the waveforms of the burst catalog fit completely in the window, while only the last cycles of the inspiral, merger and ringdown of the BBH waveforms are taken into account to perform the denoising. This late part of the BBH signal is arguably the most interesting part, hence deserving to be denoised best. Below we comment on the reason for this choice and on existing alternatives to also reconstruct the early inspiral part of the signal.

To ensure the best conditions for the convergence of the algorithms and to avoid round-off errors, we also scale the amplitude of the validation signals of both catalogs so that their maximum value is set to unity. The values of the regularization parameter λ we discuss in this section are hence determined by this normalization. Moreover, we scale each signal to achieve a specified value of the SNR, defined as

$$\text{SNR} = \sqrt{4\Delta t^2 \Delta f \sum_{k=1}^{N_f} \frac{|\tilde{h}(f_k)|^2}{S(f_k)}}, \quad (4.1)$$

where \tilde{h} indicates the Fourier transform of signal strain h , S is the power spectral density (PSD) of the noise, i.e. the sensitivity curve of the detector, f_k is each of the components of

the frequency vector, N_f is the number of positive frequencies, and Δt and Δf are the time step and frequency step, respectively.

The optimal value of the regularization parameter, λ_{opt} , is defined to be the one which gives the best results according to a suitable metric function applied to the denoised signal and the original one, measuring the quality of the recovered signal. In our case we choose two estimators, namely the Mean Squared Error,

$$\text{MSE} = \frac{1}{n} \sum_{i=1}^n (\hat{Y}_i - Y_i)^2, \quad (4.2)$$

where \hat{Y} and Y are the reconstructed and original signals, respectively, and n is the number of samples, and the structural similarity (SSIM) index [57], which deviates from the traditional measures of error because it takes into account the structural information. The SSIM index varies between 0 (minimum similarity) and 1 (maximum similarity) and is defined as

$$\text{SSIM}(x, y) = \frac{(2\mu_x\mu_y + c_1)(2\sigma_{xy} + c_2)}{(\mu_x^2 + \mu_y^2 + c_1)(\sigma_x^2 + \sigma_y^2 + c_2)}, \quad (4.3)$$

where c_1 and c_2 are constants, μ_x (μ_y) is the average of x (y), σ_x^2 (σ_y^2) the variance of x (y) and σ_{xy} the covariance of x and y .

As mentioned before we use 80% of the signals of each catalog to produce one dictionary per type of signal. To do the learning, we select 30000 random patches (the starting sample is random) of a selected length, which is a parameter to be estimated. The patches are selected uniformly from all the learning waveforms of each catalog. Then, we select the p patches with the highest energy, defined as the square of the L^2 -norm of each patch. After that, we solve problem (2.12) using a block-coordinate descent method. This step is done modifying the code developed by [58]. Fig. 1 shows a small representation of the atoms of both dictionaries.

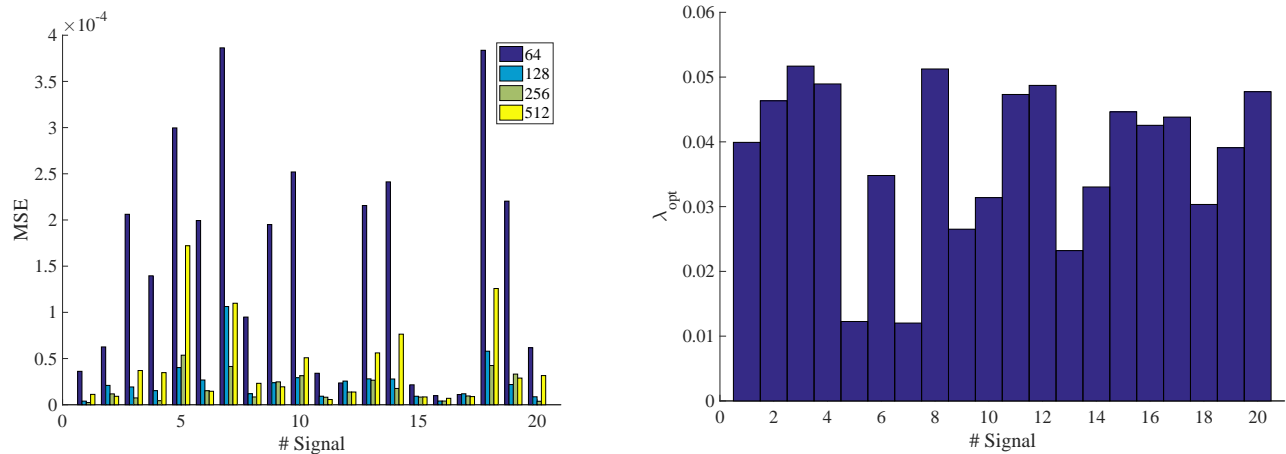


FIG. 2: *Left:* Bar diagram of the MSE for all burst validation signals. Each color represents a different window length as indicated in the legend. *Right:* Bar diagram of the optimal value of λ for all burst validation signals and a window length $n = 256$. The mean value of λ_{opt} is 0.038 ± 0.018 .

In addition to the search of λ_{opt} we must decide the best values for the size of the dictionary, i.e. the number of atoms and their length. To this aim we calculate the MSE for the reconstructed signals obtained using dictionaries of different sizes. In each case, the value λ_{opt} will be the corresponding value that minimizes the MSE. For this task we use the validation set of signals of the dictionaries and set the SNR to 20. As the length of the atoms is always shorter than the length of the validation signals, we do the denoising with a sliding window with an overlap of $n - 2$ samples, where n is the length of the window, which agrees with the length of the atoms. With this overlap, there are many samples that are repeated on different windows. These samples must be averaged to obtain the final reconstructed signals. Our initial tests show that the best reconstruction is achieved using TV-averaging (see [59]),

$$s = \frac{\sum_{j=1}^p (f_j \text{TV}_j)}{\sum_{j=1}^p \text{TV}_j}, \quad (4.4)$$

where f_j corresponds to the current patch and $\text{TV}_j = \sum |\nabla f_j|$ is the Total-Variation norm of that patch.

B. Parameter evaluation

We calculate the MSE for the validation set of burst signals with window lengths $l = 64, 128, 256,$ and 512 . The results are shown in the left panel of Fig. 2. Each vertical bar represents the value of the MSE for each atom length. The figure shows that the largest value of the MSE is achieved for a length of 64. This is due to the fact that if the atoms are too short the reconstructed signal is more oscillatory due to the noise. This effect can be corrected using larger lengths. However, the larger the length of the atoms the more difficult to recover the smallest oscillations of the original signal. This is the reason why the MSE actually grows for the larger window length analyzed (512 samples). While this is a generic

trend, it is nevertheless still possible that the longest window may work better for specific signals (e.g. signals #6 or #11 in Fig. 2). However, in general the best results correspond to a length of 256 samples.

The right panel of Fig. 2 displays the values of λ_{opt} , i.e. the value of the regularization parameter that minimizes the MSE value. It has been obtained for a fixed window length $l = 256$. This figure reveals that the values of λ are bounded between 0.01 and 0.06. Therefore, not all values of λ are possible and selecting the mean value $\lambda_{\text{opt}} = 0.03$ will produce, on average, a good reconstruction for all burst signals. Nevertheless, fine-tuning this parameter can improve the results in specific cases.

We next carry out the same analysis for the case of BBH signals. As BBH waveforms are totally different to burst signals, the choices just discussed for bursts would not lead to satisfactory results if applied blindly to the BBH catalog. Contrary to burst signals, BBH waveforms are significantly longer, therefore we need to increase the length of the atoms. The values obtained for the MSE for the BBH catalog are shown in the left panel of Fig. 3 and correspond to atom lengths that comprise from 128 to 1024 samples. The case of 64 samples is not shown in the figure because the corresponding value of the MSE is much larger. As for the case of burst signals, Fig. 3 shows that the MSE decreases with the window length in most cases. Therefore, to denoise BBH waveform signals we select the length of 1024 samples as it produces the best results.

The corresponding results for the value of λ_{opt} for BBH are shown in the right panel of Fig. 3. Again, the values are restricted to a small interval between 0.002 and 0.012. As we show below, using the mean value, $\lambda_{\text{opt}} = 0.008$, yields to satisfactory denoising results in most cases.

A similar study is required to determine how the results depend on the *number* of atoms of the dictionary p . In general, the larger the dictionary the better the results, but at a higher computational cost. Therefore, setting the size of the dictionary is often a trade-off between results quality and effi-

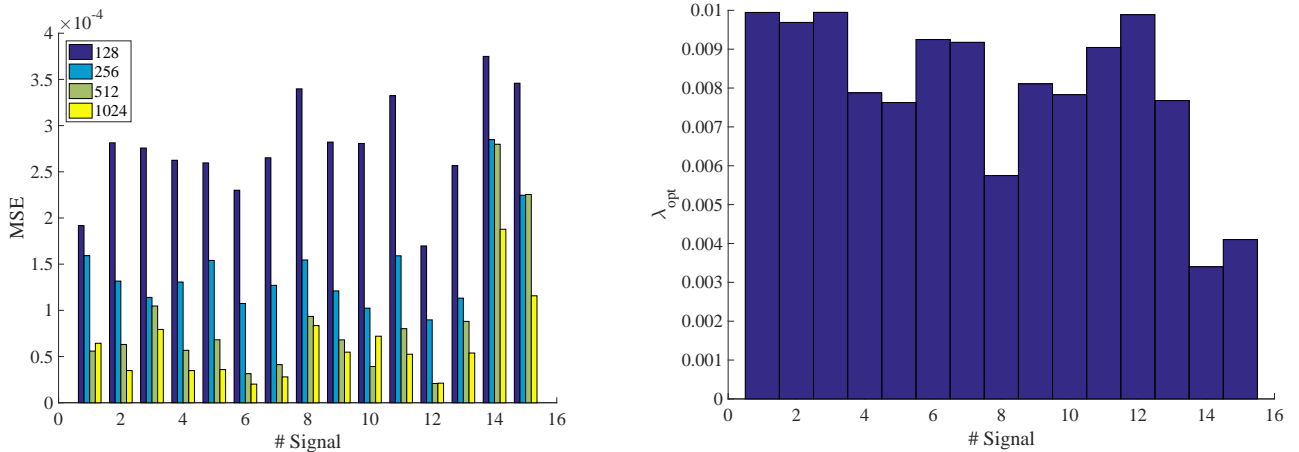


FIG. 3: *Left*: Bar diagram of the MSE for all the BBH validation signals. Each color represents a different window length as shown in the legend. *Right*: Bar diagram of the optimal value of λ for all the BBH validation signals and a window of length 1024. The mean value of λ_{opt} is 0.008 ± 0.002 .

ciency. To evaluate an optimal value for the number of atoms we carry out tests with the two catalogs using values from $p \in \{300, 500, 1000\}$ in the case of bursts with $n = 256$ atom length and from $p \in \{1100, 2000, 2500\}$ in the case of BBH with $n = 1024$ atom length. We find that using 500 and 1100 atoms for bursts and BBH, respectively, is a valid compromise as it produces good results at a reasonable computational cost. However, if computational resources are not an issue, there is no reason not to use larger dictionaries. For the two catalogs, the value of λ_{opt} for $p = 500$ and $p = 1100$ atoms are bounded in a similar interval than shown before.

V. TESTS AND RESULTS

A. No signal

The first test consists in studying the performance of the method when there is no signal inside the data set. The goal of this test is to check if in the absence of signal the dictionary produces spurious signals due to noise. The result of this test is shown in Fig. 4. A stream of 0.5 s of pure non-white Gaussian noise (upper panel) is denoised using the generic value of λ_{opt} corresponding to burst signals, i.e. $\lambda_{\text{opt}} = 0.03$. One can see that the resulting signal has zero amplitude throughout the frame (lower panel) for this specific value of λ . This is the ideal behavior of the algorithm in order to avoid false detections due to noise.

We next repeat this test for 200 independent realizations of noise (following the procedure outlined in Appendix A of [37]) to check if this behavior remains the same irrespective of the noise realization. For our specific value of λ we find 26 false reconstructions due to noise fluctuations. We note however that the smaller the λ the more coefficients of the representation become nonzero and more structures due to noise may appear. In contrast, a large value of λ will reduce the ratio of false reconstructions, even though a true GW signal

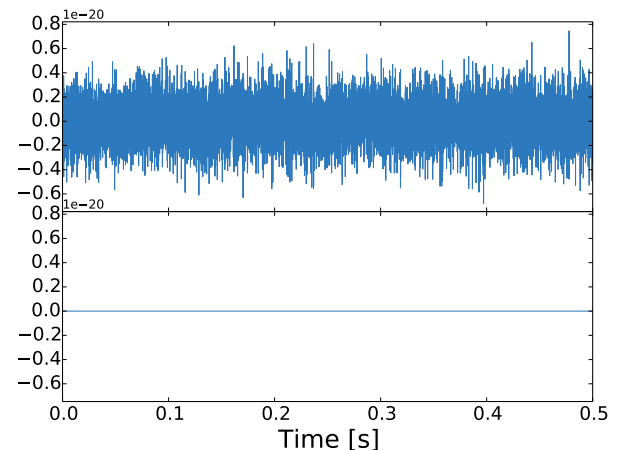


FIG. 4: Denoising with no signal embedded into Gaussian noise. The upper panel shows the original noisy signal while the lower panel shows the ideal result of the denoising, i.e. a zero amplitude signal.

with low SNR could be missed. For instance, for $\lambda = 0.045$ we only obtain one false reconstruction.

The results reported in this section are illustrative of the typical response of the LASSO algorithm on λ . A comprehensive statistical study of the dependence of the number of false reconstructions and signal misses on the parameters of the method, i.e. value of λ , type of signal injection, SNR, and noise realization, deserves further analysis. We also note that this is a fairly simple test because the noise is purely Gaussian. In a more realistic scenario, the presence of instrumental glitches in the detector data [12, 13] could produce false reconstructions.

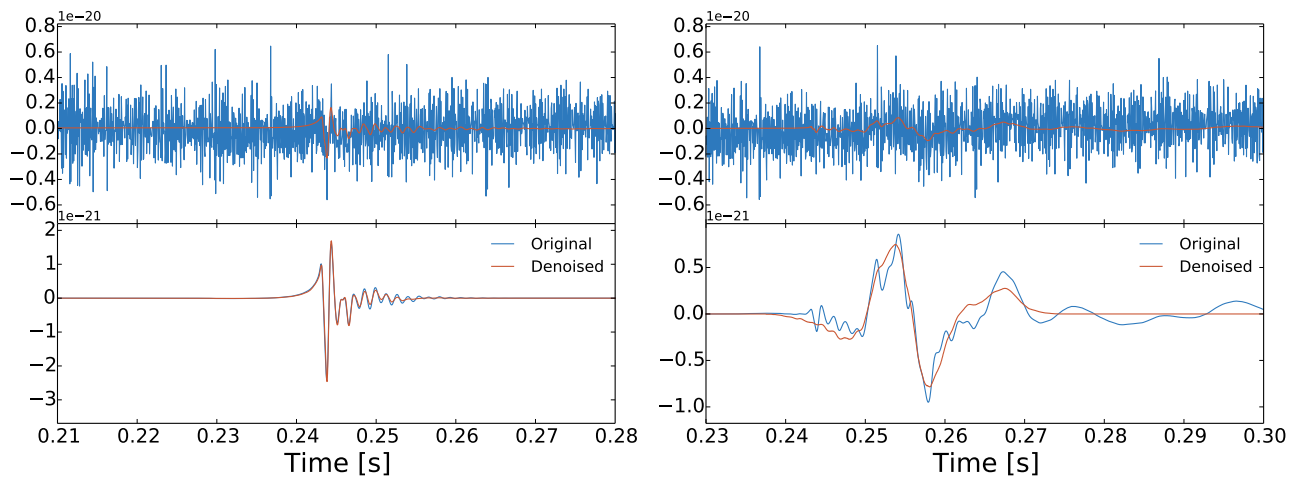


FIG. 5: Denoising of signal #1 (left) and #6 (right) from the group of test signals of the burst catalog. The time of arrival is random and the SNR is 20. Upper panels: noisy signals (blue) superimposed with the original numerical relativity waveforms (red). Lower panels: comparison between the denoised signals (red) with the original ones (blue). The MSE and SSIM values are 0.018×10^{-3} and 0.98 for the signal on the right panel and 0.271×10^{-3} and 0.67 for the signal on the left panel.

B. Signals from the catalogs

Next we study how the method works when applied to the eight test waveform signals of the burst catalog in a long data frame. In the figures for this and the following tests, we use the same noise realization to compare the results on an equal footing. Correspondingly, in the tables reported in this section, we present results obtained with 20 different noise realizations to find out how the reconstruction is affected by noise fluctuations. The signals are embedded in Gaussian noise with a SNR of 20. The time of arrival is fixed and it is the same for all the signals. The value of the regularization parameter is set to $\lambda = 0.03$ and remains the same value for all the tests of this section. Although this value is not the optimal one, i.e. the one which produces the best results for a given signal, our goal is to determine if it is possible to recover the signal with a generic value of λ . This approach may be closer to what occurs in a realistic situation, where no information on the signal is available a priori.

The quality of the denoising is measured using the MSE and the SSIM metric functions, and is reported in Table I for all test signals. This table shows the maximum and the minimum values for both MSE and SSIM for 20 independent noise realizations. We recall that the results depend on the value of λ . Each signal embedded in different noise realizations is a new scenario, and the best results will be obtained with the optimal value of λ for each case. With SNR 20 and $\lambda = 0.03$ the relative variations are not too large (the highest variation in SSIM is 14% for signal #6). Therefore, at this SNR, the reconstruction is not very affected by noise fluctuations. Fig. 5 shows the results for only two signals of the catalog, namely those which yield the best (signal #1; left panel) and the worst (signal #6; right panel) denoising results, respectively (for the chosen value of λ and noise realization). The figure displays the comparison of the two original noisy signals (upper

panels) with the recovered ones (lower panels). Concerning the signal on the left panel our method can accurately recover the distinctive positive and negative peaks associated with the hydrodynamical bounce that follows the collapse of the inner iron core of the star once the equation of state stiffens and the central density exceeds nuclear matter density. This is particularly clear for the peaks with the larger amplitudes, which are recovered properly. However, when the amplitude decreases (i.e. in the part of the temporal evolution associated with the quasi-radial oscillations of the newly formed neutron star) the signal becomes weaker than the noise and, as a result, the method returns a zero amplitude signal. It is also worth mentioning that in the part of the time series where the data are purely noise (no numerical relativity signal injected) the method returns a zero signal, as it should. The same behavior is seen for the signal displayed on the right panel of Fig. 5, the dampened oscillations are weaker than the noise and the method sets their amplitude to zero. We note that signal #6 is somewhat different from the common features of the dictionary. As a result, while the broad morphology is still captured to some extent, the overall result is poorer than for the signal on the left panel. Even so, we note that the results can be improved by changing slightly the value of λ by adding more atoms to the dictionary. (We have checked that for $\lambda = 0.026$ the MSE is 0.1×10^{-3} and the SSIM is 0.77.)

To find out the dependence of the procedure on the SNR we reduce its value from 20 to 10, keeping the same value of λ . The results are displayed in Fig. 6 for the same signals #1 and #6 of the burst catalog. The results for all test signals and the corresponding maximum and minimum measures of the MSE and SSIM are also reported in Table I. Figure 6 shows that for SNR 10 signal #1 is still very well recovered and its most significant features can be reconstructed with relatively high accuracy. The MSE for this signal increases an order of magnitude and the SSIM decreases from 0.98 to 0.91, still reasonably high. For the worst possible case of the test wave-

TABLE I: Values (maximum - minimum) of the MSE and SSIM error estimators for the eight burst signals we use as test signals and 20 noise realizations. Values are reported for both SNR 20 and 10.

Signal	SNR 20		SNR 10	
	MSE ($\times 10^{-3}$)	SSIM	MSE ($\times 10^{-3}$)	SSIM
#1	[0.033 - 0.015]	[0.97 - 0.93]	[1.389 - 0.021]	[0.96 - 0.74]
#2	[0.124 - 0.030]	[0.95 - 0.85]	[1.264 - 0.125]	[0.89 - 0.60]
#3	[0.066 - 0.040]	[0.93 - 0.88]	[0.691 - 0.073]	[0.89 - 0.74]
#4	[0.068 - 0.007]	[0.97 - 0.88]	[0.684 - 0.014]	[0.95 - 0.74]
#5	[0.052 - 0.022]	[0.94 - 0.89]	[1.335 - 0.041]	[0.90 - 0.53]
#6	[0.210 - 0.084]	[0.83 - 0.72]	[0.861 - 0.205]	[0.72 - 0.51]
#7	[0.130 - 0.083]	[0.90 - 0.84]	[2.350 - 0.103]	[0.88 - 0.43]
#8	[0.042 - 0.016]	[0.93 - 0.85]	[0.594 - 0.026]	[0.91 - 0.74]

forms, signal #6, Fig. 6 shows that it can still be distinguished from the noise.

Comparing the results for all burst signals reported in Table I for SNR 20 and SNR 10, we see that, in general, the values of the MSE (SSIM) increase (decrease) if the SNR decreases, except for the case of signal #6. We recall that we are using the same value of λ for all signals, and if it is not near the optimum value for any given signal, the results will not be good. In the case of signal #6 the errors for SNR 20 are actually slightly worse than for SNR 10. As the SNR decreases, the reconstruction is more affected by noise fluctuations and the difference between the maximum and minimum values of the quality indicators increases. As we have mentioned before, other values of λ could improve the results in each case.

We turn next to test the results from the BBH catalog. As these signals are much longer than burst signals, the total segment of data has a length of 2 s, in order to allow to change the time of arrival. In this case, it is set as the time where the merger is produced, randomly. The denoising results are reported in Table II for all BBH signals and displayed in Fig. 7 for a representative signal (#2). As the figure shows, the signal is properly denoised during its three distinctive parts, the inspiral, the merger, and the ringdown. In particular, the phase of the signal is well captured and the main, yet small, differences between the original and the denoised signal appear in the amplitude. We note that the actual signal is significantly longer than the zoom shown in this figure. The initial part of the signal, the inspiral phase with low frequencies, is not recovered because, as mentioned before, the dictionary is specifically designed to recover the merger part. The most striking incorrect feature of Fig. 7 is the presence of spurious oscillations visible after the ringdown. This is due again to the selection of λ . While using a larger value would remove these oscillations it is also possible that the amplitudes of the merger and ringdown parts of the signal could be cut down. The corresponding MSE and SSIM measures are reported in Table II for both SNR 20 and 10. As for the case of burst waveforms, for BBH signals the values of the MSE (SSIM) also increase (decrease) as the SNR decreases, as expected.

TABLE II: Values (maximum - minimum) of the MSE and SSIM error estimators for the four BBH signals we use as test signals and 20 noise realizations. Values are reported for both SNR 20 and 10.

Signal	SNR 20		SNR 10	
	MSE ($\times 10^{-3}$)	SSIM	MSE ($\times 10^{-3}$)	SSIM
#1	[0.025 - 0.019]	[0.89 - 0.86]	[0.084 - 0.027]	[0.87 - 0.76]
#2	[0.060 - 0.027]	[0.86 - 0.79]	[0.104 - 0.039]	[0.83 - 0.66]
#3	[0.029 - 0.020]	[0.88 - 0.87]	[0.101 - 0.032]	[0.86 - 0.74]
#4	[0.034 - 0.019]	[0.89 - 0.86]	[0.101 - 0.025]	[0.87 - 0.74]

C. Signals not included in the catalogs

In a realistic scenario, the gravitational wave signal will be unknown and it will be contaminated by several sources of noise. To test the code in a more unidealized setting we select in this section signals with similar broad morphology to those of the dictionaries but generated in a different way (e.g. employing different numerical codes or input physics). While such a situation is still simple, since it involves simulated Gaussian noise without glitches, it is nonetheless more realistic because, contrary to the cases analyzed before, the signals are now different from those of the catalogs from which the dictionaries are generated.

We first consider a burst signal from a core collapse catalog generated by [52]. We select signal #1 from this catalog, embed it into Gaussian noise with a SNR 20, and proceed to denoise it employing our burst dictionary. The results of the denoising are displayed in Fig. 8. This figure shows that the positive and negative peaks associated with core bounce are well recovered. The values of the MSE and SSIM error estimates are respectively 3.78×10^{-5} and 0.96. Notwithstanding some characteristics of the signal are lost, the signal can nevertheless be clearly distinguished from the noise and the main features are well recovered.

We can carry out a similar study for our BBH dictionary. As mentioned before, we select the BBH signal ‘R1’ from [53]. The result of the denoising is displayed in Fig. 9 which shows that the reconstruction is much less accurate than in the case of the BBH test signals discussed before. We obtain $\text{MSE} = 5.79 \times 10^{-4}$ and $\text{SSIM} = 0.55$, values which indicate a poor reconstruction. The merger is not correctly recovered and the reconstruction introduces a phase shift. We must recall once again that we are using a generic value of λ and therefore the result could be significantly improved by choosing a more suitable value. However, the goal of this test is not to obtain the best result possible but to assess our procedure in a scenario where the incoming signal is unknown and differs from those used to train the dictionary.

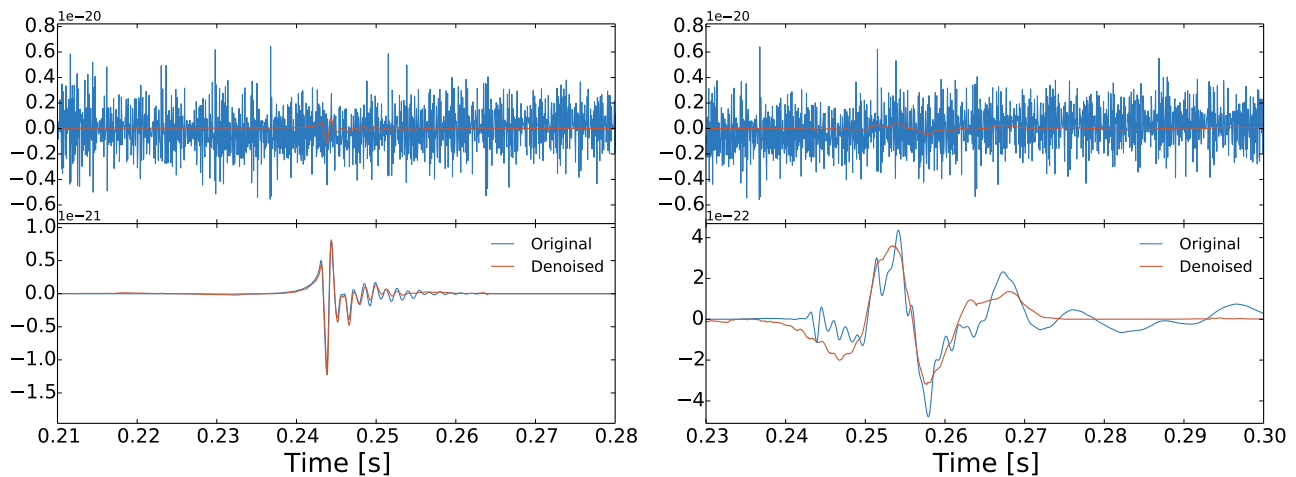


FIG. 6: Same as Fig. 5 but with SNR 10. The MSE and SSIM values are 0.081×10^{-3} and 0.91 for the signal on the right panel and 0.20×10^{-3} and 0.71 for the signal on the left panel.

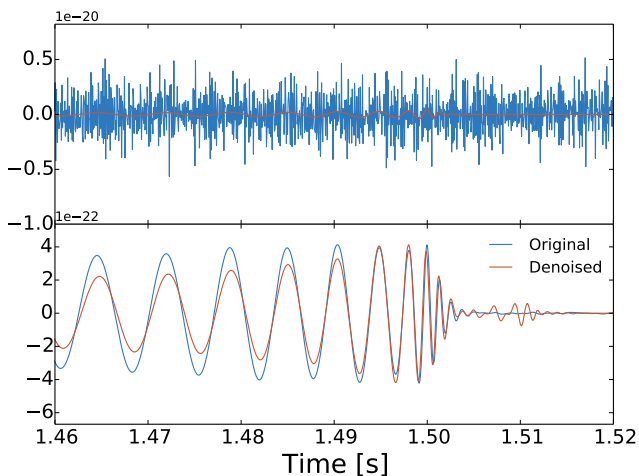


FIG. 7: Denoising of the test signal #2 taken from the BBH catalog. The SNR is set to 20 in a 2 s frame. The value of λ used is 0.01 with TV averaging. The values of MSE and SSIM are 0.031×10^{-3} and 0.86 respectively.

VI. COMPLEMENTARY TESTS

A. Iterative denoising

The next situation we consider involves a simple direct extension of the method, namely using the denoising procedure in an iterative way. By removing noise iteratively we find that the small amplitude oscillations of the signals are recovered better than using one single iteration. In this approach we use a generic, low value of λ , which only removes a small amount of noise in every iteration. We apply this iterative approach to burst signal #6 with SNR 20. The results are shown in Fig. 10 (to be compared with the right panel of Fig. 5). For this SNR we find that typically only 2 or 3 iterations suffice to recover the small amplitude oscillations of the signal and improve the

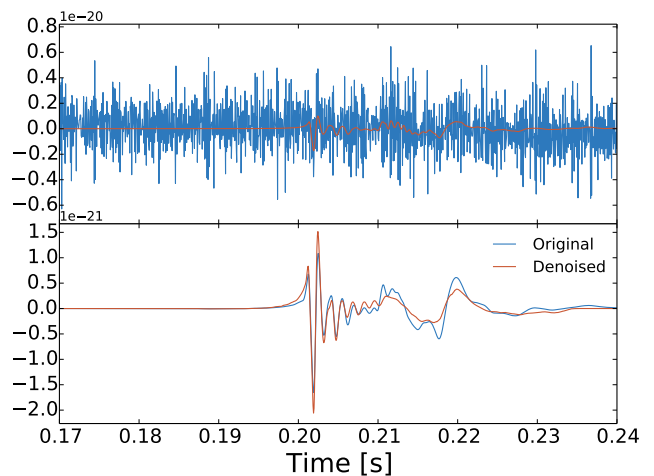


FIG. 8: Denoising of a burst signal from the core collapse catalog of [52] using a dictionary generated from a different catalog [43]. The arrival time is random, the SNR is 20 and $\lambda = 0.03$.

results. For this test we obtain $\text{MSE} = 0.079 \times 10^{-3}$ and $\text{SSIM} = 0.81$. These values are considerable better than those reported in Table I for the case of a single iteration.

B. Combination of signals

For our next test we assess our procedure when the signal to denoise is a combination of two different signals. The goal of this test is to check the performance of our dictionaries when dealing with signals different from the type they are designed for. To do that, we build a test signal which is a combination of a burst and a BBH, both with SNR 20. We apply the algorithm using both dictionaries independently. The results of this test are shown in Fig. 11. The upper panel shows the original test signal (red line) embedded in Gaussian noise. The burst is lo-

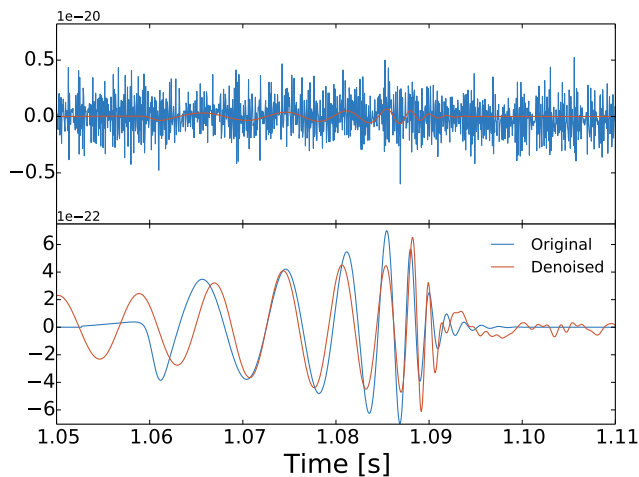


FIG. 9: Denoising of the ‘R1’ BBH signal computed by the GSFC group [53] using a dictionary trained with signals from a different catalog [5]. The SNR is set to 20 and the time of arrival is random in a 2 s frame. The value of λ used is 0.09 with TV averaging.

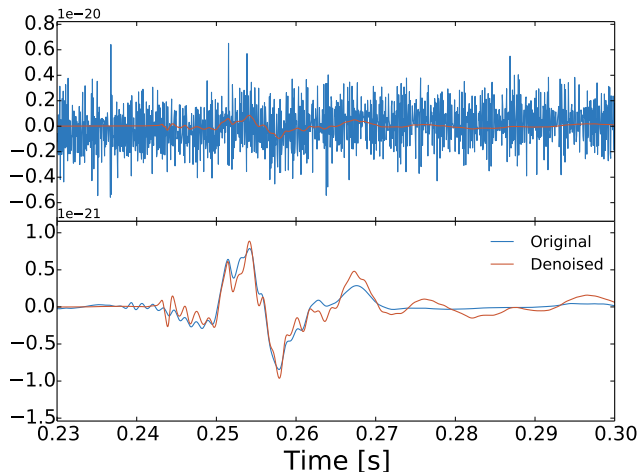


FIG. 10: Denoising of signal #6 of the burst catalog employing an iterative procedure with only 2 iterations. We choose $\lambda = 0.01$ and SNR 20.

cated around $t \sim 1.34$ s while the merger of the BBH signal is visible at $t \sim 1.50$ s. The middle panel shows the reconstruction (red line) using only the burst dictionary with a value of $\lambda = 0.03$. The inset of this panel zooms around the time of the burst and subsequent oscillations of the proto-neutron star. Correspondingly, the lower panel displays the results of the denoising using only the BBH dictionary with a value of $\lambda = 0.01$. Clearly each dictionary discriminates well between the type of signal it has been designed to search for, despite both signals overlap in time. When using the burst dictionary the method returns no BBH signal, as can be seen in the middle panel. Likewise, when using the BBH dictionary, no burst signal is visible in the lower panel, and the late inspiral and merger parts of the BBH signal are recovered properly. The discrepancies in the early inspiral and the spurious oscillations

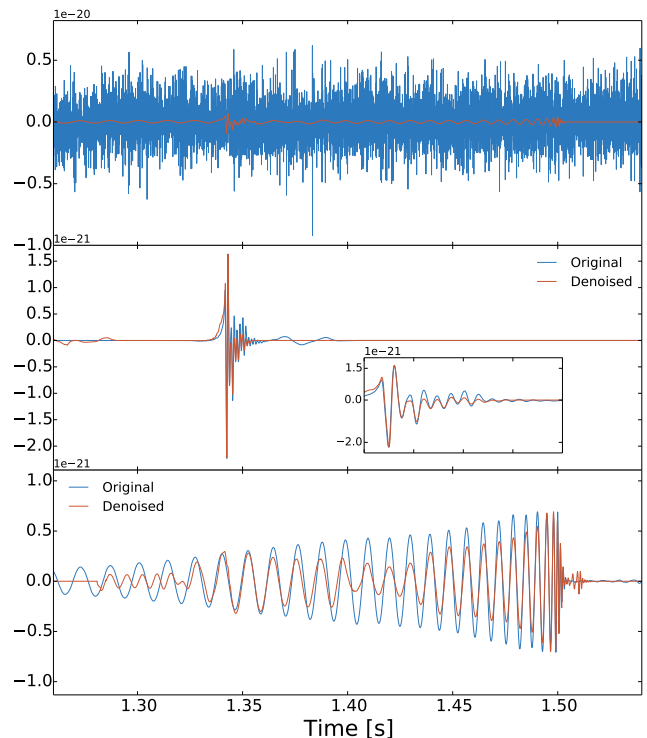


FIG. 11: Denoising of a test signal composed by a combination of burst signal #5 and BBH signal #2. The individual signals are independently recovered when using the appropriate dictionary in a standalone way, as shown in the middle and bottom panels.

after the ringdown are to be expected, as we have explained before.

C. Low SNR scenario

The following test we consider is a low SNR scenario, namely SNR 6. Our strategy to denoise the signal in such a challenging situation consists in using the dictionary in combination with spectrograms, a common tool in data analysis. This test has two main goals. On the one hand, it allows us to check if our denoising procedure can improve the results of the spectrogram. On the other hand, we can test if the dictionary can recover the signal with acceptable accuracy in a low SNR scenario, once the time of arrival is known thanks to the spectrogram. We proceed as follows. First we apply the dictionary denoising with a generic value of λ , namely $\lambda = 0.02$. Its value should be lower than that for SNR 20 to allow to recover the signal and also part of the noise. Then we calculate the spectrogram and select a window around the time of the maximum power (integrated over all frequencies). This step is a simple version of the event trigger generator implemented on the detectors [60]. Next, we apply the iterative denoising procedure to this small window. In this case, we select the number of iterations that minimizes (maximizes) the MSE (SSIM) values. We have observed that the dependence of these values with the number of iterations does not follow

a convex distribution. Therefore, it is unfortunately difficult to find a general rule which gives information on what is the best number of iterations.

The results are shown in Fig. 12 for signal #1 of the burst catalog. The middle panel of this figure displays the spectrogram. The denoised signal shown in the lower panel after applying our two-step procedure clearly indicates the benefits of using the combined approach. The values of the MSE (0.2×10^{-3}) and SSIM (0.88) indicate that the reconstruction is quite accurate even with this low SNR. These values are similar to those for SNR 10 reported in Table I. Therefore, the results of this test fulfill our two objectives. A key issue in this example is how to find the correct arrival time. We note that when using an even lower value of the SNR the arrival time obtained by the power integration does not always correspond to the arrival time of the signal. This issue could be solved by applying the iterative denoising directly to the list of candidate triggers.

D. LASSO selection

Up to now our experiments have focused on the goal of obtaining the best signal reconstruction for a generic value of the regularization parameter λ . In this section we show how the LASSO algorithm can also be used to infer some basic physical parameters of the sources from the denoised signals. We plan to further develop this approach towards parameter estimation in the near future.

We use the entire catalog as dictionary, except the test signals, without the learning procedure, and use the LASSO to select the signals closest to the one we use as test. The dictionary is not normalized in order to maintain the relative amplitude between the different waveforms that compose the catalog. Ideally, if a signal captured by the detector is inside the catalog, LASSO will select that signal. However, as the reconstruction is not perfect due to noise and the signal is not inside the catalog, LASSO will return the combination of signals that are more similar to the denoised one. To investigate if the selection can indeed be used to extract the physical parameters of the original signal, we devise the following procedure: firstly, we perform the denoising of the signal with a random time of arrival. We employ SNR 20 and $\lambda = 0.03$. Secondly, once we have a clean signal, we use LASSO with the catalog and obtain the corresponding coefficients of each signal. It is possible to reconstruct the waveform using these coefficients and the catalog. Therefore, the value of λ in the selection is the one that minimizes the error between the denoised signal and the reconstructed one.

As an example, the results of the parameter estimation of test signals #1 and #7 of the burst catalog are shown in Table III. The actual numbers of these two signals inside the catalog are #26 and #123 respectively. In this table the signal listed above the horizontal line is the test signal, and the next three lines indicate the corresponding three signals of the catalog with the highest LASSO coefficients (employing the original numbering of signals of the catalog). This table shows that the physical parameters of the collapse progenitors are reason-

TABLE III: Parameter estimation: comparison between the physical parameters of test signals #1 and #7 of the burst catalog. From left to right the columns report: number of catalog signal, model name, progenitor mass M , degree of differential rotation A , precollapse angular velocity at the center $\Omega_{c,i}$, precollapse rotation rate β_i , and equation of state.

Signal	Model name	M	A	$\Omega_{c,i}$	β_i	EOS
		$[M_\odot]$	$[10^8 \text{ cm}]$	$[\text{rad s}^{-1}]$	$[\%]$	
#123 (#7)	s40A3O12	40	0.5	10.65	1.84	LS
#124	s40A3O12	40	0.5	10.65	1.84	Shen
#114	s40A2O13	40	1.0	6.45	2.60	Shen
#59	s15A3O12	15	0.5	10.65	1.60	LS
#26 (#1)	s11A3O09	11	0.5	8.99	0.72	Shen
#24	s11A3O07	11	0.5	5.95	0.40	Shen
#54	s15A3O05	15	0.5	4.21	0.25	Shen
#25	s11A3O09	11	0.5	8.99	0.72	LS

ably identified, especially for test signal #123 where the only discrepancy is on the EOS. (This is however to be expected as the catalog only uses two EOS, Shen and LS, and the signal for the LS EOS is the actual test signal and is hence *removed* from the catalog.) The estimations for signal #26 are not as good but at least the differential rotation A of the progenitor is well obtained.

We turn next to estimate the parameters of test signal #2 from the BBH catalog using the same procedure as for burst waveforms. Table IV reports the correspondence between the test signal and the three signals from the BBH catalog with the highest LASSO coefficients. Again, we find a good overall agreement, being the physical parameters of the test signal and the selected ones in a similar range. The main discrepancy is found in the BH masses, M_1 and M_2 .

The mismatch observed in the parameter estimation is produced for two main reasons. On the one hand, the LASSO capabilities for parameter estimation obviously depend on how dense is the catalog. In the case of the two catalogs we employ in this work (and of most catalogs for that matter), the physical parameters are not sampled with detail due to the large computational cost of the simulations. It is likely that our results might improve when more complete catalogs become available. The second reason is due to the fact that we are using denoised waveforms as input, which includes the errors from the dictionary reconstruction. The more accurate the denoising results, the more precise the parameter estimation. However, since in a real world application the original signal is unknown, the LASSO classification can still be regarded as a useful tool to complement existing parameter estimation techniques (see e.g. [14, 61–63]).

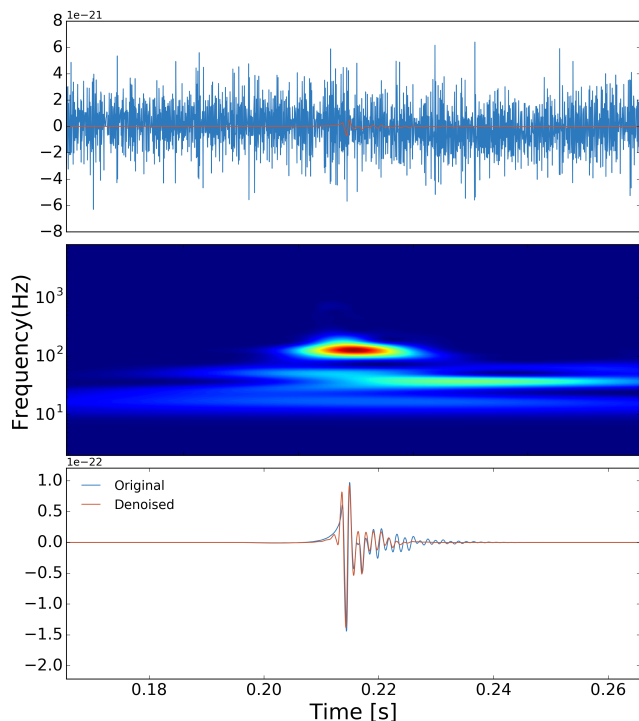


FIG. 12: Denoising of signal #1 of the burst catalog employing iterative denoising and spectrograms. The middle panel shows the spectrogram of the 0.5 s denoising with a general value of λ . The results shown at the lower panel were calculated using $\lambda = 0.0095$ with 12 iterations, and SNR 6.

TABLE IV: Parameter estimation: comparison between the physical parameters of BBH test signal #2. From left to right the columns report: number of catalog signal, initial BH separation r_0 (in units of mass), initial orbital frequency $M\omega_0$, initial expansion factor $\dot{a}_0 = \dot{r}_0/r_0$, Christodoulou masses of the two BHs at $t = 0$, orbital eccentricity ϵ , number of orbits between $t = 0$ and common horizon time, and mass of final BH (remnant) M .

Signal	r_0	$M\omega_0$	\dot{a}_0	M_1	M_2	ϵ	Orbits	M
#47	14	0.017	-0.00028	0.75	0.25	0.00047	22.7	0.96
#56	15	0.015	-0.00028	0.84	0.16	0.00049	28.8	0.98
#29	16	0.014	-0.00033	0.60	0.40	0.00044	21.6	0.95
#28	16	0.014	-0.00026	0.60	0.40	0.00016	23.8	0.94

VII. GW150914

For our final test we assess our algorithms with the real GW data of the discovery signal GW150914. We use as few assumptions about instrumental noise as possible, due to the fact that the detector noise is non-Gaussian and non-stationary. However, a minimum noise preprocessing is required due to two main reasons. On the one hand, there are well-known modeled sources of narrow-band noise (see Fig. 3 of [1]). On the other hand, ground-based detectors such as LIGO are not

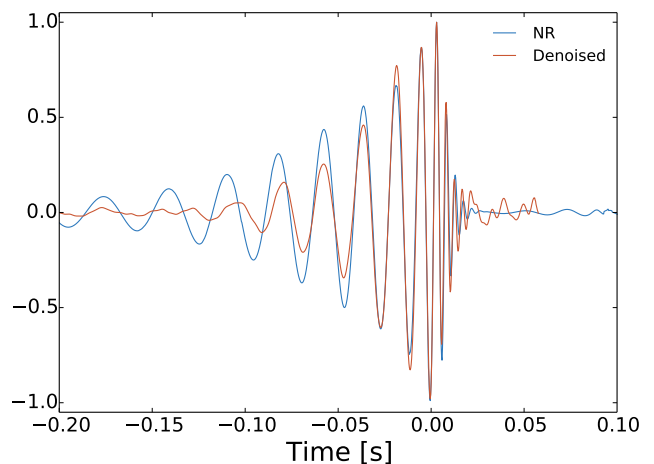


FIG. 13: Denoising of signal GW150914 detected by advanced LIGO Hanford interferometer. We choose $\lambda = 0.004$. The blue line indicates the NR template and the red curve corresponds to the actual signal. The amplitude of both signals has been rescaled to lie in the interval $[-1, 1]$.

sensitive to low frequencies because of seismic noise. Therefore, we highpass the time series above 30 Hz to remove seismic noise and, following [1], we also filter out all spectral lines.

The results of applying the dictionary denoising procedure to the GW150914 Hanford signal are shown in Fig. 13. The red curve in this figure displays the denoised signal obtained after applying the procedure to the real data. The implementation of the same approach to the best fit numerical relativity waveform [64] is shown with the blue curve. Even though the two signals are sampled at 4096 Hz, we use the high resolution dictionary as it leads to better results. This is common practice in the case of image denoising, where high resolution dictionaries are built to perform the denoising of low resolution images [40]. Fig. 13 shows that the last cycles of the inspiral signal, the merger part, and the ringdown agree well with the NR waveform. Comparing the two signals of Fig. 13 at ± 0.15 s from the minimum of the numerical relativity signal yields $\text{MSE} = 0.0075$ and $\text{SSIM} = 0.4901$. These quality measures show that while visually the comparison between both signals seems satisfactory, the reconstruction is not very accurate. A full parameter study to find the optimal values of the dictionary algorithms for signals embedded in real noise will be presented elsewhere.

VIII. SUMMARY AND OUTLOOK

In this paper we have studied the capabilities of learned dictionaries to recover GW signals from a noise-dominated background. Our LASSO algorithm has been tested using signals from two main sources, bursts from rotational core collapse and chirps from BBH coalescence. To obtain the respective dictionaries, we have used 80% of the waveforms for the training, 15% for the validation, i.e. to obtain the best set

of parameters that produces the best results, and the last 5% waveforms to assess the method. An interesting feature of LASSO is that, for most Gaussian noise realizations considered, it returns zero if the input signal cannot be reconstructed by the atoms on the dictionary. As a result, the method may provide a fairly clear signal reconstruction. On the other hand, an intrinsic limitation of the method is that the results strongly depend on the selection of the regularization parameter λ , whose optimal value cannot be set a priori, and must be obtained with validation studies. It is possible that, if some noise transient (glitch) is similar to an actual GW signal, the method may be able to reproduce it and produce a false reconstruction. We defer for a future study the analysis of the false alarm rate using simulated (or real) glitches. We believe that this analysis, together with validation studies using real noise, are mandatory before using dictionaries in a detector's pipeline. To avoid false positives caused by glitches, it is possible to apply our method employing dictionaries built from a collection of known glitches. This idea follows the line of research proposed by [12, 13].

Our results demonstrate that it is possible to extract GW signals embedded in Gaussian noise with good accuracy, using a generic dictionary with a common value of λ for each type of waveforms. Overall, our results show that the denoising procedure works better for bursts than for BBH signals. This can be due to two main reasons. First, the morphology and the duration of both signals are very different. In particular, in the case of BBH signals, significantly longer than bursts, we need more atoms to cover all the signal duration. The second reason is related to the trained dictionary itself. The atoms on the burst dictionary are quite different between them which allows to cover more signal morphologies with a combination of only a few of them (sparse representation). In contrast, the atoms on the BBH dictionary are much more homogeneous since the signals used to train the dictionary are similar in the inspiral phase and only differ more clearly at the merger and the ringdown parts. Therefore, most of the atoms of the BBH dictionary cover the inspiral part, which can be reconstructed more easily. The larger inaccuracies appear when recovering the merger and the ringdown signals because there are less atoms to cover these parts and the reconstruction is less adaptable. A possible solution to this issue could be to use a couple of dictionaries, one to cover the inspiral part and a second one to cover only the merger and the ringdown parts. This may be worth investigating in the future. In addition, we have shown that using the LASSO algorithm iteratively can improve the results. Once a collection of triggers (i.e. arrival times) is available, it is possible to obtain the signal in a few iterations even for low SNR values. However, in order to determine the number of iterations that produces the optimal results, a more detailed study is necessary.

We have also reported results on the use of the LASSO algorithm as a classification method (i.e. for parameter estimation). The classification depends on how dense is the catalog and on how much noise can be removed from the original signal. The results become more accurate the larger the col-

lection of waveforms available in the catalogs and the larger the physical parameters those catalogs cover, which is a major computational task. In particular, in the case of burst signals from core-collapse, the computational cost involved in calculating the GW waveforms renders unfeasible to obtain a large enough template bank. This classification method has therefore the same limitations than matched filtering. Even so, using the LASSO algorithm as a classification method deserves attention, particularly if used jointly with matched filtering techniques. Finally, we have also briefly shown the performance of dictionary-learning techniques for actual GW signals under real noise conditions. The results for the discovery signal GW150914 seem promising.

There exist a large variety of learning techniques in the literature. In the present work we have only considered one specific method but in the near future we plan to implement additional methods to perform the learning and to compute the LASSO algorithm more efficiently. Obtaining the denoised solution for one patch of 256 samples takes typically a few tens of ms on an Apple iMac computer with Intel Core i7 processor and 16 Gb of Ram. The most expensive computational cost is associated with the learning task. Reducing the time involved in this part of the method is a key issue in order to eventually apply the method in real time to the actual data generated by the detectors. In the next few months, advanced LIGO and advanced Virgo will (re)start observing runs with improved sensitivity, increasing the number of detections. The development of sophisticated data analysis techniques to improve the opportunities of detection, especially for low SNR events, is therefore a most crucial effort. The study reported in this work has shown that if the data are in good enough agreement with the morphology of the atoms used to produce the dictionary, dictionary-learning algorithms may be used to extract signals from noise and to infer physical parameters. These algorithms could thus be a complementary addition to the gravitational wave data analysis toolkit.

Acknowledgements

We thank the anonymous referee whose constructive review helped to improve the manuscript. Work supported by the Spanish MINECO (grants AYA2013-40979-P and MTM2014-56218-C2-2-P) and by the Generalitat Valenciana (PROMETEOII-2014-069).

Appendix A: Correspondence with signal catalogs

For the sake of completeness and to facilitate the identification of the NR waveforms used in this study, Table V reports the correspondence of the waveforms of our two dictionaries with the original naming of the burst [43] and BBH [5] signal catalogs.

TABLE V: Relation between the number of the GW signals employed in the validation set (first two columns) and in the test set (last two columns) with the corresponding signal in the core-collapse catalog [43] and in the BBH catalog [5].

#	Validation		Test	
	Core Collapse	BBH (SXS)	Core Collapse	BBH (SXS)
#1	S15A2O13_shen	SXS:BBH:0022	S11A3O09_shen	SXS:BBH:0030
#2	S15A3O07_ls	SXS:BBH:0003	S15A1O09_ls	SXS:BBH:0047
#3	S15A3O15_shen	SXS:BBH:0028	S15A1O09_shen	SXS:BBH:0068
#4	S15A2O13_ls	SXS:BBH:0076	S15A3O15_ls	SXS:BBH:0087
#5	S15A1O01_ls	SXS:BBH:0001	S20A2O07_shen	
#6	S20A1O09_shen	SXS:BBH:0077	S40A1O01_shen	
#7	S11A1O01_shen	SXS:BBH:0090	S40A3O05_ls	
#8	S40A2O15_ls	SXS:BBH:0053	S40A3O12_ls	
#9	S20A2O05_ls	SXS:BBH:0019		
#10	S20A1O09_ls	SXS:BBH:0041		
#11	S15A2O07_ls	SXS:BBH:0091		
#12	S20A3O07_ls	SXS:BBH:0050		
#13	S11A2O07_ls	SXS:BBH:0080		
#14	S11A1O13_ls	SXS:BBH:0062		
#15	S15A2O05_ls	SXS:BBH:0059		
#16	S11A3O13_shen			
#17	S11A3O09_ls			
#18	S40A1O01_ls			
#19	S11A1O05_shen			
#20	S20A3O13_shen			

- [1] B.P. Abbott et al., Phys. Rev. Lett. **116**, 061102 (2016).
[2] B.P. Abbott et al., Phys. Rev. Lett. **116**, 241103 (2016).
[3] M. Campanelli, C. O. Lousto, P. Marronetti, and Y. Zlochower. Phys. Rev. Lett. **96**, 111101 (2006).
[4] Signal SXS:BBH:0305, available at URL <http://www.black-holes.org/waveforms>.
[5] A.H. Mroué et al, Phys. Rev. Lett. **111**, 241104 (2013).
[6] Advanced Virgo Baseline Design,” The Virgo Collaboration, VIR-0027A-09 (2009); available from <https://pub3.ego-gw.it/itf/tds/>
[7] Y. Aso, Y. Michimura1, K. Somiya2, M. Ando, O. Miyakawa, T. Sekiguchi, D. Tatsumi, H. Yamamoto, and (The KAGRA Collaboration), Phys. Rev. D **88**, 043007 (2013).
[8] B.P. Abbott et al., Living Rev. Relativity **19**, 1 (2016).
[9] D. V. Martynov, et al. arXiv preprint arXiv:1604.00439 (2016).
[10] J. Abadie et al. Phys. Rev. D **85**, 122007 (2012).
[11] N. Christensen (LIGO and Virgo Scientific Collaborations). Class. Quantum Grav. **27**,194010 (2010).
[12] J. Powell, D. Trifirò, E. Cuoco, I.S. Heng and M. Cavaglià. Class. Quantum Grav. **32**, 215012 (2015).
[13] J. Powell, A. Torres-Forné, R. Lynch, D. Trifirò, E. Cuoco, M. Cavaglià, I.S. Heng, and J.A. Font. arXiv:1609.06262 (2016).
[14] P. Jaranowski and A. Królak, ”Gravitational-Wave Data Analysis. Formalism and Sample Applications: The Gaussian Case”, Living Rev. Relativity **15**, (2012), 4. URL (cited on 7-20-2016): <http://www.livingreviews.org/lrr-2012-4>
[15] A. Buonanno and T. Damour, Phys. Rev. D **62**, 064015, (2000).
[16] L. Blanchet, T. Damour, B.R. Iyer, C. M. Will, and A. G. Wiseman, Phys. Rev. Lett. **74**, 3515, (1995).
[17] L. Blanchet, T. Damour, G. Esposito-Farèse, and B.R. Iyer, Phys. Rev. Lett. **93**, 091101, (2004).
[18] A. Nagar and L. Rezzolla, Class. Q. Grav. **22**, R167 (2005).
[19] B.J. Owen and B. S. Sathyaprakash, Phys.Rev. D **60**, 022002,(1999).
[20] B.S. Sathyaprakash and B.F. Schutz, ”Physics, Astrophysics and Cosmology with Gravitational Waves”, Living Rev. Relativity **12**, (2009), 2. URL (accessed 7-15-2016): <http://www.livingreviews.org/lrr-2009-2>
[21] B.P. Abbott et al., arXiv:1606.04856 (2016).
[22] B.P. Abbott et al., Phys. Rev. Lett. **116**, 241102 (2016).
[23] S. Bose, A. Pai, and S. V. Dhurandhar, Int. J. Mod. Phys. **D 9**, 325 (2000).
[24] S. Klimenko, SI Yakushin, A. Mercer and G. Miselmakher. Class. Quantum Grav. **25**. 114029 (2008).
[25] C. Palomba (for the LIGO and VIRGO Scientific Collaborations), arXiv:1201.3176 [astro-ph.IM].
[26] P. Cerdá-Durán, N. DeBrye, M.A. Aloy , J.A. Font and M. Obergaulinger, ApJ, **779**, L18 (2013).
[27] T. Damour and A. Vilenkin, Phys. Rev. **D71**, 063510 (2005).
[28] B. P. Abbott et al., Phys. Rev. **D 93**, 042005 (2016).
[29] B.P. Abbott et al. Rep. Prog. Phys. **72** 076901(2009).
[30] E. Thrane and M. Coughlin, Phys. Rev.Lett. **115**, 181102 (2015).
[31] S. Klimenko et al. Phys. Rev. **D 93**, 042004 (2016).

- [32] J. B. Kanner et al. *Phys. Rev.* **D93**, 022002 (2016).
- [33] T. B. Littenberg, J. B. Kanner, N. J. Cornish, and M. Millhouse, arXiv:1511.08752.
- [34] R. Lynch, S. Vitale, R. Essick, E. Katsavounidis, and F. Robinet, arXiv:1511.05955.
- [35] C. Röver, M.A. Bizouard, N. Christensen, H. Dimmelmeier, I.S. Heng, and R. Meyer, *Phys. Rev. D* **80**, 102004 (2009).
- [36] W. J. Engels, R. Frey and C. D. Ott. arXiv:1406.1164 [gr-qc] (2014).
- [37] A. Torres, A. Marquina, J.A. Font, J.M. Ibáñez. *Phys. Rev D* **90** (8), 084029 (2014).
- [38] L.I. Rudin, S. Osher and E. Fatemi, *Physica D* **60** 259-268. North-Holland, (1992).
- [39] S.C. Chen, D.L. Donoho and M.A. Saunders. *SIAM*. Vol. 43, No. 1, pp. 129-159. (2001).
- [40] M. Elad and M. Aharon. *Image Processing, IEEE Transactions on*, 15(12), 3736-3745 (2006).
- [41] J. Mairal, F. Bach and J. Ponce. *Pattern Analysis and Machine Intelligence, IEEE Transactions on*, 34(4), 791-804 (2013).
- [42] S. Mallat and Z. Zhang. *IEEE Transactions on Signal Processing*, **41**, 3397 (1993).
- [43] H. Dimmelmeier, C. D. Ott, A. Marek, and H.-T. Janka, *Phys. Rev. D* **78**, 064056 (2008).
- [44] B.A. Olshausen and D.J. Field. *Vision Research*, **37**, 3311-3325 (1997).
- [45] M. Aharon, M. Elad, and A. Bruckstein. *Image Processing, IEEE Transactions on*, 54(11), 4311-4322 (2006).
- [46] M.W. Marcellin, M.J. Gormish, A. Bilgin and M.P. Boliek. *Proc. Data Compression Conf.* (2000)
- [47] R. Tibshirani, *J. of the Royal Statistical Society. Series B*, vol. 58, 267-288 (1996).
- [48] H. Zou and T. Hastie, *Journal of the Royal Statistical Society Series B*, vol 67, no 2 (2005).
- [49] T. Goldstein and S. Osher, *J. Imag. Sci.* **2** 323-43. (2009)
- [50] P. Tseng, *J. Optim. Theory Appl.*, 109, 475-494 (2001).
- [51] J. Mairal, F. Bach, J. Ponce and G. Sapiro. In *Proceedings of the 26th annual international conference on machine learning* (pp. 689-696). ACM. (2009).
- [52] E. Abdikamalov, S. Gossan, A. M. DeMaio, and C. D. Ott, *Phys. Rev. D*, **90**, 044001 (2014).
- [53] J. G. Baker, M. Campanelli, F. Pretorius, and Y. Zlochower, *Class. Quantum Grav.* **24**, S25 (2007).
- [54] <http://www.black-holes.org/SpEC.html>
- [55] <http://astrograv.gsfc.nasa.gov/docs/waveforms/NRmergers/>
- [56] J. Creighton et al. *LAL software documentation* (2007), URL <http://www.lsc-group.phys.uwm.edu/daswg/projects/lal.html>.
- [57] Z. Wang, A. C. Bovik, H. R. Sheikh, and E. P. Simoncelli, *IEEE Transactions on Image Processing*, Volume 13, Issue 4, pp. 600-612, (2004).
- [58] G. Peyré, *The Numerical Tours of Signal Processing - Advanced Computational Signal and Image Processing IEEE Computing in Science and Engineering*, vol. 13(4), pp. 94-97, (2011).
- [59] A. Marquina and S. Osher, *J. Sci. Comput.*, **37**, 367-382. (2008).
- [60] B.P. Abbott et al. *Phys. Rev. D* **93**, 122004 (2016).
- [61] B.P. Abbott et al. *Phys. Rev. D* **94**, 064035 (2016).
- [62] J. Logue, C.D. Ott, I.S. Heng, P. Kalmus, and J.H.C. Scargill, *Phys. Rev. D* **86**, 044023 (2012).
- [63] N.J. Cornish and T.B. Littenberg, *Class. Quantum Grav.* **32**, 135012 (2015).
- [64] B. Abbott et al, <https://doc.ligo.org/LIGO-P1500218/public/main>.